JGR Space Physics

RESEARCH ARTICLE
10.1029/2020JA028705

Key Points:

- We demonstrate use of Spatio-Temporal Difference (STD) and polynomial reconstruction to determine the 2-D velocity of a magnetic structure
- Velocities from STD and reconstruction roughly agree with each other and with estimates from other references for the July 11, 2017 event
- Polynomial reconstruction is most likely to be accurate within a distance of 2 spacecraft spacings from the centroid of the Magnetospheric Multiscale spacecraft

Supporting Information:

- Supporting Information S1
- Movie S1
- Movie S2
- Movie S3
- Movie S4

Correspondence to:
R. E. Denton,
richard.e.denton@dartmouth.edu

Citation:
Denton, R. E., Torbert, R. B., Hasegawa, H., Genestreti, K. J., Manuzzo, R., Belmont, G., et al. (2021). Two-dimensional velocity of the magnetic structure observed on July 11, 2017 by the Magnetospheric Multiscale spacecraft. *Journal of Geophysical Research: Space Physics*, *126*, e2020JA028705. https://doi.org/10.1029/2020JA028705

Received 11 SEP 2020
Accepted 13 FEB 2021

Two-Dimensional Velocity of the Magnetic Structure Observed on July 11, 2017 by the Magnetospheric Multiscale Spacecraft

Richard E. Denton[1], Roy B. Torbert[2], Hiroshi Hasegawa[3], Kevin J. Genestreti[4], Roberto Manuzzo[5,6], Gerard Belmont[5], Laurence Rezeau[5], Francesco Califano[6], Rumi Nakamura[7], Jan Egedal[8], Olivier Le Contel[5], James L. Burch[9], Daniel J. Gershman[10], Ivan Dors[2], Matthew R. Argall[2], Christopher T. Russell[11], Robert J. Strangeway[11], and Barbara L. Giles[10]

[1]Department of Physics and Astronomy, Dartmouth College, Hanover, NH, USA, [2]Institute for the Study of Earth, Oceans, and Space, University of New Hampshire, Durham, NH, USA, [3]Institute of Space and Astronautical Science, JAXA, Sagamihara, Japan, [4]Institute for the Study of Earth, Oceans, and Space, Southwest Research Institute, Durham, NH, USA, [5]LPP, CNRS, Ecole Polytechnique, Sorbonne Université, Observatoire de Paris, Université Paris-Saclay, PSL Research University, Paris, France, [6]Department of Physics E. Fermi, Università di Pisa, Pisa, Italia, [7]Space Research Institute, Austrian Academy of Sciences, Graz, Austria, [8]Department of Physics, University of Wisconsin-Madison, Madison, WI, USA, [9]Space Science and Engineering Division Southwest Research Institute, San Antonio, TX, USA, [10]NASA Goddard Space Flight Center, Greenbelt, MD, USA, [11]Institute of Geophysics and Planetary Physics, University of California at Los Angeles, Los Angeles, CA, USA

Abstract In order to determine particle velocities and electric field in the frame of the magnetic structure, one first needs to determine the velocity of the magnetic structure in the frame of the spacecraft observations. Here, we demonstrate two methods to determine a two-dimensional magnetic structure velocity for the magnetic reconnection event observed in the magnetotail by the Magnetospheric Multiscale (MMS) spacecraft on July 11, 2017, Spatio-Temporal Difference (STD) and the recently developed polynomial reconstruction method. Both of these methods use the magnetic field measurements; the reconstruction technique also uses the current density measured by the particle instrument. We find rough agreement between the results of our methods and with other velocity determinations previously published. We also explain a number of features of STD and show that the polynomial reconstruction technique is most likely to be valid within a distance of 2 spacecraft spacings from the centroid of the MMS spacecraft. Both of these methods are susceptible to contamination by magnetometer calibration errors.

1. Introduction

In magnetic reconnection, plasma flows toward the magnetic X line (a magnetic null in the reconnection plane, in which it appears as an X point) with an inflow velocity and is accelerated and ejected in an orthogonal direction with an outflow velocity because of the large curvature of the magnetic field in the vicinity of the X line (e.g., Sonnerup, 1979; Vasyliunas, 1975). To determine these velocities, one needs to determine the frame of reference in which the X line is stationary. Thus an important part of the process of understanding a magnetic reconnection event is to determine the velocity of the magnetic structure relative to the observing spacecraft. Although on large scales, plasma may be "frozen in" to the magnetic field, at least in directions perpendicular to the magnetic field, this is typically not the case on small scales close to the X line, especially in the region known as the electron diffusion region (Hesse et al., 2011, 2014).

Shi et al. (2019) has reviewed methods to determine a coordinate system and magnetic structure velocity. Methods to determine the velocity include calculating the deHoffmann-Teller frame in which the electric field is approximately zero, various types of timing analysis, various reconstruction methods, and the Spatial-Temporal Difference (STD) method (Shi et al., 2006). STD has been used by Denton et al. (2016a, 2016b) and Yao et al. (2016, 2018) to determine the time-dependent velocity of a magnetic structure in the normal direction. Alm et al. (2017) used STD to calculate the time-dependent two-dimensional velocity of the spacecraft moving through a structure of ion-scale magnetopause flux ropes. Manuzzo et al. (2019)

described difficulties with calculating the structure velocity in multiple dimensions, and suggested new approaches to calculate the velocity. Their method includes the possibility of including mild time dependence. The implementation of STD that we will describe in this study is somewhat simpler and assumes that the structure velocity is constant on the timescale of motion across the spacecraft separation, as did the original STD.

Recently Torbert, Burch, Argall, et al. (2018) and Torbert et al. (2020) introduced a new method for reconstruction of the instantaneous magnetic field in the region close to the Magnetospheric Multiscale (MMS) spacecraft using a polynomial expansion of the magnetic field with input from the spacecraft measurements of the magnetic field and particle current density. Denton et al. (2020) described a number of variations of Torbert and coworker's method and tested the validity of the magnetic field model during times in which the magnetic structure was roughly two dimensional. In this study, we will use Denton and coworker's Reduced Quadratic model that results from the assumption that $\lambda_1 \gg \lambda_2 \gg \lambda_3$, where λ_i are the eigenvalues of Minimum Directional Derivative (MDD) analysis that determines the eigenvectors of the gradient of the vector magnetic field (Shi et al., 2005).

We will apply our implementation of STD to calculate the velocity of the magnetic structure for the magnetotail reconnection event on July 11, 2017 described by Torbert, Burch, Phan, et al. (2018). In the process, we will elucidate several aspects of STD. Then we will use the polynomial reconstructions to get a second estimate of the velocity by following the motion of the reconstructed reconnection X point. We show that these velocity estimates are roughly in agreement with each other, at least when the reconnection X point is within about two spacecraft separations of the centroid of the MMS spacecraft, and thereby validate the reconstructed magnetic field at locations within that distance.

Most of our results will be presented in a way that assumes that the reconnection geometry is approximately two dimensional. There are a number of methods that can be used for defining a reconnection coordinate system (e.g., Denton et al., 2018; Genestreti et al., 2018). While the normal direction for the July 11, 2017 event is fairly well determined, there is significant uncertainty about the best definition of the remaining directions, since different methods lead to different results (Genestreti et al., 2018). We will initially present results in a coordinate system based on MDD analysis (Shi et al., 2005, 2019), because, for reasons that we will explain below, that is the best coordinate system for testing our methods. But as discussed in Section 4, there are good reasons to consider other coordinate systems. So we will also show results in one of the coordinate systems preferred by Genestreti et al. (2018). This will also facilitate comparison to calculations of the structure velocity by other researchers.

The study is organized as follows. In Section 2, we describe the data and methods to be used, in Section 3, we calculate the velocity of the magnetic structure using the two methods, and in Section 4, we discuss our results, including comparison to previous estimates of the structure velocity based on other methods.

2. Data and Methods

2.1. MMS Data

In this study, we will examine the magnetotail reconnection event on July 11, 2017 at 22:34 UT. The time t will be measured in seconds after this time. This event was first studied by Torbert, Burch, Phan, et al. (2018) and has been the subject of a number of other studies (e.g., Egedal et al., 2019; Genestreti et al., 2018; Hasegawa et al., 2019; Nakamura et al., 2019). The position of the spacecraft was in the magnetotail at [−21.53, 4.23, 3.64] R_E in geocentric solar ecliptic (GSE) coordinates. The average separation between spacecraft was 18.3 km.

For context, Figure 1 shows plasma and field data from MMS3, which came closest to the reconnection X line for times surrounding the time interval that we will be concentrating on, t = 1.6–2.8 s, marked by the two vertical gray lines in each panel. This time interval was close to a magnetic minimum that was observed just after t = 2.8 s. Figure 1b shows that during t = 1.6–2.8 s, B_X (in GSE coordinates) changed from negative values to a value close to zero, suggesting that MMS3 was approaching the current sheet from the south. The variation of B_Z (Figure 1b) suggests that the magnetic structure was moving tailward, so that, relative to that structure, the MMS spacecraft skimmed past the reconnection X line nearly along but southward of

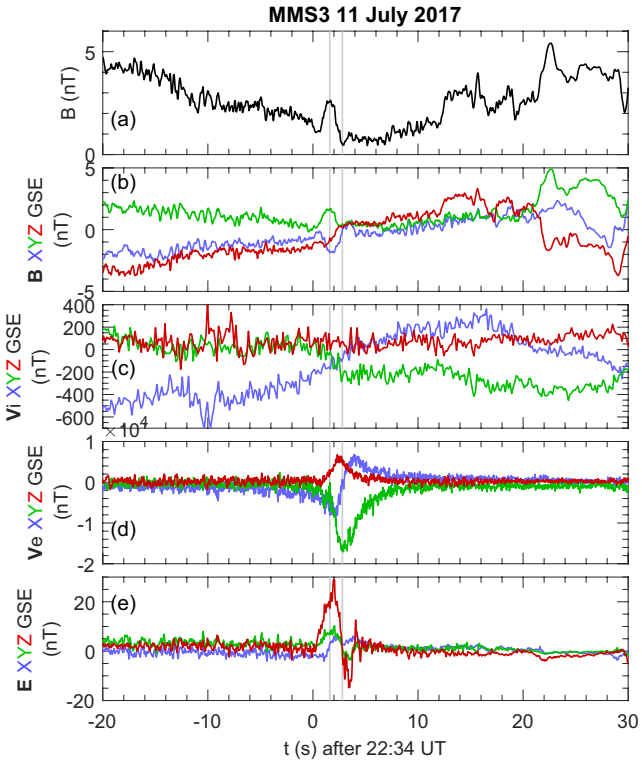

Figure 1. Plasma and field values measured by MMS3 for times surrounding our event on July 11, 2017. (a) Magnitude of the magnetic field **B**, (b) vector components of **B**, (c) vector components of the ion velocity $\mathbf{V}_i$, (d) vector components of the electron velocity $\mathbf{V}_e$, and vector components of the electric field **E**, all at 30 ms resolution in GSE coordinates versus time in seconds after 22:34 UT on July 11, 2017. GSE, geocentric solar ecliptic.

the current sheet. The reversal of the X component of ion velocity $\mathbf{V}_i$ (Figure 1c) and electron velocity $\mathbf{V}_e$ (Figure 1d) is evidence of reconnection outflow, and an intense current density (Y component of $\mathbf{V}_e$ in Figure 1d) and electric field near the current sheet (Figure 1e) is also evident.

As discussed by Denton et al. (2020), we use the magnetic field and particle current density from the MMS mission (Burch et al., 2015). The fluxgate magnetometer (FGM) (Russell et al., 2016) and search coil magnetometer (SCM) (Le Contel et al., 2016) data are combined into a single product with original resolution of 0.12 ms (Argall et al., 2018; Fischer et al., 2016). We boxcar average this to 1 ms resolution. We calculate the particle current density, **J**, from the burst mode ion and electron bulk velocity moments from the Fast Plasma Instrument (FPI) (Pollock et al., 2016), using the formula $\mathbf{J} = en_e'\left(\mathbf{V}_i - \mathbf{V}_e\right)$, where e is the proton charge, n_e' is an adjusted electron density, and $\mathbf{V}_i$ and $\mathbf{V}_e$ are respectively the ion and electron bulk velocity. Within the time interval 1.6 –3.1 s (a slightly more complete time interval than the one we will analyze), a factor f is found at each time step such that $fn_e\left(\mathbf{V}_i - \mathbf{V}_e\right)$ averaged over the spacecraft is closest in a least squares sense to the current density obtained using the "curlometer" technique (Robert et al., 1998) (that determines the current density from $\nabla \times \mathbf{B}/\mu_0$ using the spacecraft **B** values and spatial separations). During t = 1.6 –3.1 s, the values of f varied between 0.65 and 1.13. The quantity n_e' is the median value of f for the time series, 0.844, multiplied by the observed n_e. This adjustment was made because particle instruments typically do not accurately measure all particles, so $\mathbf{J}_{curl}$ is considered to be more accurate than **J**. But using the constant in time median value of f allowed for the possibility of real time variation of **J** averaged over the spacecraft. The effect of this adjustment is discussed more in Section 4.

The resolution of the electron moments was 30 ms, and that of the ions (measured collectively) was 150 ms. To combine the numerical data in the calculations, we need to interpolate all of them to the same temporal grid. For this grid, we choose a resolution of 1 ms, which is somewhat lower than that of the highest resolution magnetic field data. This procedure leads to oversampling of most data. However, all the results are finally boxcar averaged to 0.5 s resolution, so none of the data are effectively over-sampled. The purpose of this procedure is to focus on the low-frequency behavior and filter out wave phenomena. Despite the smoothing, use of the combined FGM/SCM magnetometer product reduces noise relative to that found using the burst mode data, probably by reducing the error associated with interpolating the individual MMS spacecraft field values (with different timestamps) to common times.

Because of this averaging, our methods are likely to be accurate only in some average sense on a timescale ≤0.5 s. Our reconstruction technique has previously revealed some significant time dependence (Denton et al., 2020), and here we again find time variation in the structure velocity using both STD and the polynomial reconstruction (Figure 4a). There may very well be more detailed short timescale behavior that we do not describe.

We examine how our results vary with respect to some variations in data processing in Section 4.

2.2. Structure Velocity From STD

The Spatio-Temporal Difference (STD) method of Shi et al. (2006) is based on the convection equation,

$$\frac{d\mathbf{B}}{dt} = \frac{\partial \mathbf{B}}{\partial t} + \mathbf{V}_{sc} \cdot \nabla \mathbf{B}, \quad (1)$$

where $\mathbf{V}_{sc}$ is the velocity of the spacecraft relative to the magnetic structure and $d\mathbf{B}/dt$ is the rate of change of the magnetic field observed at the spacecraft. Shi et al. neglected the partial time derivative relative to the convective term (see Manuzzo et al., 2019, for a method to take this into account) to get

$$\frac{d\mathbf{B}}{dt} = -\mathbf{V}_{str} \cdot \nabla \mathbf{B}, \tag{2}$$

where $\mathbf{V}_{str} = -\mathbf{V}_{sc}$ is the structure velocity relative to the spacecraft. This equation can be solved as a set of simultaneous equations at the resolution of the magnetometer data, yielding time-dependent structure velocities.

Assume that an event *L-M-N* coordinate system has been established (Denton et al., 2018; Genestreti et al., 2018, and references therein). Usually we want L to be the direction of the reconnection magnetic field; N may be the normal direction across the current sheet, and M is the remaining direction. In the common two-dimensional description of magnetic reconnection, M is assumed to be the direction of invariance, but sometimes the most invariant direction has a different orientation than that of M if the L direction is determined based on maximum variance of $\mathbf{B}$ (Denton et al., 2016a, 2018).

A local time-dependent coordinate system *l-m-n* is based on the eigenvectors of MDD analysis (Shi et al., 2005). In MDD, a symmetric tensor is formed by multiplying the gradient of the vector magnetic field by its transpose, and then the eigenvectors of the resulting symmetric tensor are found. In this case, n corresponds to the maximum gradient direction, m corresponds to the minimum gradient direction, and l corresponds to the intermediate gradient direction (The definitions of l and m are reversed from those recently used by Manuzzo et al. (2019)). If the coordinate system is time invariant, the *l-m-n* coordinate system would be the same as the event coordinate system *L-M-N* if the gradient is a minimum in the M direction. Below, l, m, or n as a subscript will indicate a component, and as a variable will indicate a component of a position vector, similar to the way that x, y, and z are often used.

As described by Shi et al. (2006), and further in Appendix A, we can solve Equation 2 for the local gradient k (l, m, or n) component of the structure velocity, $\mathcal{V}_{\mathrm{str,k}}$, using

$$\mathcal{V}_{\mathrm{str,k}} = -\mathcal{B}_{dt,i}\, \mathcal{G}_{k,i} / \lambda_k, \tag{3}$$

where $\mathcal{B}_{dt,i}$ is the i component of the time derivative of $\mathbf{B}$ as observed by the spacecraft, $\mathbf{G} = \nabla \mathbf{B}$, λ_k is one of the MDD eigenvalues, the calligraphy letters indicate that the quantities are in the local gradient (*l-m-n*) coordinates system, and repeated indices are summed. Expanding this out explicitly,

$$\mathcal{V}_{\mathrm{str},k} = -\frac{1}{\lambda_k}\left(\frac{d\mathcal{B}_n}{dt}\frac{\partial \mathcal{B}_n}{\partial \mathcal{X}_k} + \frac{d\mathcal{B}_l}{dt}\frac{\partial \mathcal{B}_l}{\partial \mathcal{X}_k} + \frac{d\mathcal{B}_m}{dt}\frac{\partial \mathcal{B}_m}{\partial \mathcal{X}_k}\right), \tag{4}$$

where $\mathcal{X}$ is the position vector in the MDD eigenvector frame. From Equation 4, we see that the dominant source of $\mathcal{V}_{\mathrm{str},k}$ is from the term $\mathcal{B}_i$ for which the product of its time derivative and spatial gradient in the $\mathcal{X}_k$ direction is the greatest.

For example, suppose that we can define a reconnection *L-M-N* coordinate system for which the largest variation is for B_L and the largest spatial variation is in the N direction (Denton et al., 2018). Then $\lambda_n \approx \left(\partial B_L / \partial X_N\right)^2$, and Equation 4 would become

$$V_{\mathrm{str},N} \approx -\frac{\left(dB_L / dt\right)\left(\partial B_L / \partial X_N\right)}{\left(\partial B_L / \partial X_N\right)^2} \sim -\frac{dX_N}{dt}. \tag{5}$$

(The minus sign is because the left-hand side of Equation 5 is the structure velocity, but dX_N/dt on the right hand side of Equation 5 is the time derivative of the spacecraft displacement relative to the structure).

In the following text, we will drop the calligraphy notation, so, for instance, $V_{str,n}$ is the structure velocity in the local MDD n direction.

2.3. Reduced Quadratic Polynomial Reconstruction Model

As discussed by Denton et al. (2020), the 3D Reduced quadratic (RQ-3D) model was found by starting with the full quadratic expansion of the vector magnetic field in the local MDD l-m-n coordinate system (three-dimensional polynomial expansion with up to second derivatives, including mixed terms like $\partial^2 B_l/\partial l \partial n$), and then reducing the number of terms based on the ordering $\partial/\partial n \gg \partial/\partial l \gg \partial/\partial m$. Because $\partial/\partial m$ is assumed to be small, we only allow "strictly linear" variation with respect to m. That is, the m-dependent terms are linear in m, and do not have l or n dependence. Then the m derivatives will be everywhere constant and therefore no greater than those determined from the linear gradients based on the MMS inter-spacecraft magnetic field variation. Although $\partial/\partial n$ is usually large compared to $\partial/\partial l$ and $\partial/\partial m$, we expect $\partial B_n/\partial n$ to be small because of $\nabla \mathbf{B} = 0$, so we also neglect $\partial^2 B_n/\partial n^2$ to ensure that $\partial B_n/\partial n$ remains small away from the spacecraft locations. This leads to neglect of other terms, as described in more detail by Denton et al. (2020). The resulting model is

$$B_l = B_{l,0} + \frac{\partial B_l}{\partial n} n + \frac{\partial B_l}{\partial l} l + \frac{\partial B_l}{\partial m} m + \frac{\partial^2 B_l}{\partial n^2} \frac{n^2}{2} \tag{6}$$

$$B_m = B_{m,0} + \frac{\partial B_m}{\partial n} n + \frac{\partial B_m}{\partial l} l + \frac{\partial B_m}{\partial m} m + \frac{\partial^2 B_m}{\partial n^2} \frac{n^2}{2} + \frac{\partial^2 B_m}{\partial n \partial l} nl + \frac{\partial^2 B_m}{\partial l^2} \frac{l^2}{2} \tag{7}$$

$$B_n = B_{n,0} + \frac{\partial B_n}{\partial n} n + \frac{\partial B_n}{\partial l} l + \frac{\partial B_n}{\partial m} m + \frac{\partial^2 B_n}{\partial l^2} \frac{l^2}{2} \tag{8}$$

Neglecting the displacement current in the Ampere-Maxell law, $\mu_0 \mathbf{J}$ is the curl of Equations 6–8, which is written out in Appendix B (Here μ_0 is the permeability of free space).

In addition to these equations, we have a constraint in order to ensure $\nabla \cdot \mathbf{B} = 0$. Taking the divergence of (6–8), we find

$$\frac{\partial B_n}{\partial n} + \frac{\partial B_l}{\partial l} + \frac{\partial B_m}{\partial m} = 0 \tag{9}$$

The three equations in Equations 6–8 can be solved at each spacecraft location, leading to 12 equations. Similarly the equations for $\mu_0 \mathbf{J}$ in Appendix B also yield 12 equations. With Equation 9, there are a total of 25 equations that can be used to solve for 17 parameters for a best least squares fit. A more detailed description of the method is given by Denton et al. (2020).

3. Results

3.1. MDD Analysis

Figure 2 shows the results of MDD and Minimum Gradient Analysis (MGA), both applied to the vector magnetic field (Shi et al., 2019). Figure 2a shows the eigenvalues for MDD, which are also the same as the eigenvalues for MGA (MGA will be described below). Figures 2b–2d show the local (time-dependent) MDD eigenvectors l, m, and n, respectively, expressed in terms of the global coordinates that we have chosen for this event, L-M-N. As one can see from Figures 2b–2d, l, m, and n are approximately equal to L, M, and N, respectively. In fact, $\mathbf{e}_N$ and $\mathbf{e}_M$ were found by taking the mean components of $\mathbf{e}_n$ and $\mathbf{e}_m$, making a slight adjustment of $\mathbf{e}_M$ so that it was perpendicular to $\mathbf{e}_N$, and then getting $\mathbf{e}_L$ from the cross product, $\mathbf{e}_M \times \mathbf{e}_N$. The local $\mathbf{e}_n$ direction is found from the maximum gradient eigenvector, representing the direction of the maximum gradient across the current sheet. The local $\mathbf{e}_m$ direction was the direction of the minimum gradient, so that an approximate two-dimensional representation of this system would include variation only in the N and L directions.

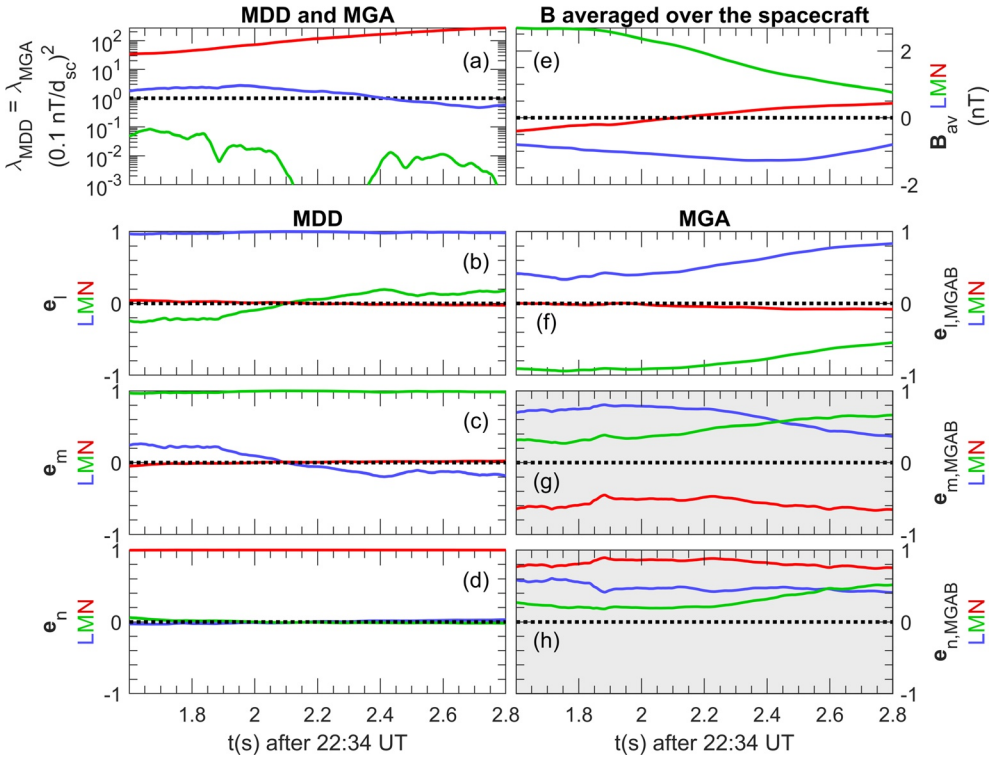

Figure 2. Minimum Directional Derivative (MDD) and Minimum Gradient Analysis (MGA). (a) MDD (or MGA) eigenvalues; (b–d) local MDD *l*, *m*, and *n* eigenvectors, respectively, with blue, green, and red curves showing the *L*, *M*, and *N* components, where [*L*; *M*; *N*] = [0.876,0.424,−0.230; −0.476,0.835,−0.275; 0.075,0.351,0.936] in GSE; (e) *L*-*M*-*N* components of the magnetic field averaged over the MMS spacecraft; (f–h) local MGA eigenvectors in the same format as for MDD. The grayed out panels are shown for completeness, but not discussed.

Note that the *l* and *L* directions based on MDD might not well represent the Minimum Variance Analysis (MVA) direction of maximum variance of the magnetic field (Sonnerup & Cahill, 1967; Sonnerup & Scheible, 1998), which is often associated with *L* (e.g., Denton et al., 2018). MGA is related to MDD in that the eigenvalues are calculated from the same tensor that is based on $\nabla \boldsymbol{B}$. But whereas for MDD the eigenvectors are sorted according to the directions of maximum and minimum gradient, for MGA the eigenvectors are sorted to find the directions of maximally and minimally varying magnetic field component (Shi et al., 2019). Therefore MGA, which finds the directions of maximum and minimum variance from the magnetic field vectors measured by the four spacecraft at one time, is "MVA-like" (Shi et al., 2019) and functions like a local (time-dependent) version of MVA. An apparently equivalent procedure to implementing MGA is to create a series of four magnetic field measurements from the four spacecraft, and then implementing MVA on that series of data points. In Figures 2f–2h, $\mathbf{e}_{l,\mathrm{MGA}}$, $\mathbf{e}_{m,\mathrm{MGA}}$, and $\mathbf{e}_{n,\mathrm{MGA}}$ are respectively the MGA maximum, intermediate, and minimum variance directions. Figure 2f shows that $\mathbf{e}_{l,\mathrm{MGA}}$ is at first mostly in the −*M* direction (green curve with largest absolute value). Later in the interval, there is more variation in the *L* direction (blue curve with largest absolute value).

We will first examine this event using the *L*-*M*-*N* coordinate system based on MDD as described above, with [*L*; *M*; *N*] = [0.879,0.419,−0.230; −0.472,0.837,-0.277; 0.077,0.352,0.933] in GSE coordinates. These coordinate directions differ by 15°, 16°, and 7°, respectively, from the *L*, *M*, and *N* directions of Torbert, Burch, Phan, et al. (2018), and by 40°, 39°, and 11°, respectively, from the hybrid MDD-B/MVA-v_e *L*, *M*, and *N* directions of Genestreti et al. (2018) (coordinate system 14 in their Table A1, with [L_G; M_G; N_G] = [0.948,−0.255,−0.189; 0.182,0.925,−0.335; 0.260,0.283,0.923] in GSE).

3.2. Velocity From STD

Equation 4 shows that the kth component of the structure velocity in the local MDD coordinates, $V_{\mathrm{str},k}$ ($\mathcal{V}_{\mathrm{str,\,k}}$ in Equation 4), has the kth eigenvalue, λ_k, in the denominator. Thus very small values of λ_k can lead to very large values of the corresponding velocity component. In principle, if the structure were truly two-dimensional and time invariant, and λ_k became very small, the numerator of Equation 4 would also become very small, so that the resulting velocity would be well behaved. But in practice, non-two dimensionality, time dependence, and approximations and errors in the calculation of the gradients can result in small values of the denominator without correspondingly small values of the numerator. Thus very small λ_k yields what we call a "singularity," leading to unrealistically large $V_{\mathrm{str},m}$ for the minimum eigenvalue m (see discussion by Manuzzo et al., 2019; Shi et al., 2019).

Since the relative DC magnetometer calibration of the MMS spacecraft is rated to be accurate to 0.1 nT, values of λ_k below $\lambda_0 = (0.1\,\mathrm{nT} / d_{\mathrm{sc}})^2$, where d_{sc} is the average spacecraft spacing (here, 18.3 km), could be suspect (Shi et al., 2019). Calibration errors are especially serious, because they can lead to systematic (constant) error in the gradients. Figure 3 shows components of the STD structure velocity, $V_{\mathrm{str,\,k}}$, in the local MDD eigenvector directions versus the normalized eigenvalue, λ_k/λ_0. One evidence that the gradient in a direction is not being calculated accurately would be that the inferred structure velocity, $V_{\mathrm{str,\,k}}$, increases as λ_k decreases. This is because, in principle, there should not be any correlation between the velocity in a certain direction and the gradient of the magnetic field in that same direction.

Evidence of this can be seen in Figure 3. Note that the velocities of the minimum gradient component of the structure, $V_{\mathrm{str,\,min}}$ (green dots), increase with decreasing λ_k/λ_0 for $\lambda_k/\lambda_0 < 10^{-1}$, that is, for data points to the left of the red vertical dotted line in Figure 3. However, it is not clear that the velocities increase with respect to decreasing λ_k/λ_0 for larger eigenvalues than about $\lambda_k/\lambda_0 = 0.25$. Consider for instance the blue points, representing the components in the intermediate gradient direction. The smallest values of $V_{\mathrm{str,\,min}}$ occur at the smallest values of $\lambda_{\mathrm{min}}/\lambda_0$. For the time being, we are going to proceed with the assumption that the velocities measured in the intermediate gradient direction (blue points in Figure 3) are accurate. This is equivalent to assuming that eigenvalues, λ_k/λ_0, are accurately calculated if their values are greater than 0.33, that is, for data points to the right of the vertical green dashed line in Figure 3. Note also that our main attention will be for the velocity before about 2.2 s, for which λ_l/λ_0 is above unity (Figure 2a).

Figure 4 shows the results of the STD analysis. The solid curves in Figure 4a show the components of the 2D STD magnetic structure velocity formed by projection of the local n and l components onto the global N (red solid curve) and L (blue solid curve) directions. The black curves in Figures 4b–4d are the n, l, and m components of the structure velocity, respectively. Comparison of the black curve in Figure 4b with the red curve in Figure 4a, and the black curve in Figure 4c with the blue curve in Figure 4a, shows that the n and l components of the STD velocity are nearly equal to the N and L components, respectively, as suggested by Figures 2d and 2b, respectively. Figures 4b–4d show $V_{str,k}$ for $k = n$, l, or m, respectively, where the red, blue, and green curves show the contributions from the B_n, B_l, and B_m dependent terms in Equation 4, respectively. As indicated by the very large values of $V_{\mathrm{str},m}$ $V_{\mathrm{str},m}$ is often grossly inaccurate if the MDD minimum gradient (m) eigenvalue is very small. Figure 4d, which shows a singularity in $V_{\mathrm{str},m}$, is included mainly to remind the reader of this fact.

Figures 4b and 4c show some possibly unexpected results. If the spacecraft cross the entire current sheet, often the largest magnetic variation is in the B_L component, due to the strong dependence of B_L on N. Then one would expect the value of $V_{\mathrm{str},n}$ to be dominated by the contribution from the B_L-dependent terms in Equation 4, as was assumed in the derivation of Equation 5. But Figure 4b shows that the value of $V_{\mathrm{str},n}$ is dominated by the contribution from the B_m-dependent terms in Equation 4. This is because for this event the MMS spacecraft were skimming close to but under the current sheet (Hasegawa et al., 2019; Torbert, Burch, Phan, et al., 2018), so that there was little variation in B_L over the time plotted in Figure 4. From Figure 2e, we can see that B_m is larger in magnitude than B_l, and that the variation in B_m is also larger, except at the end of the time interval after about $t = 2.6$ s. Consequently, $V_{\mathrm{str},n}$ is dominated by the contributions from the B_m-dependent terms in Equation 4 (green curve in Figure 4b) up until about $t = 2.6$ s, after which the B_l-dependent terms also contribute significantly (blue curve in Figure 4b).

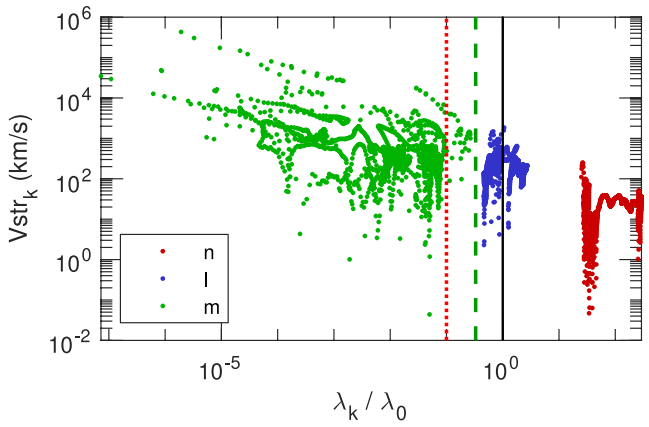

Figure 3. Velocity components in the local MDD directions versus eigenvalue. The velocity components, $V_{str,\,k}$, for the interval t = 1.6 –2.8 s are plotted versus the local normalized MDD eigenvalue, λ_k/λ_0, for the maximum gradient n component (red dots), the intermediate gradient l component (blue dots), and the minimum gradient m component (green dots), where $\lambda_0 = (0.1\,\mathrm{nT} / L_{sc})^2$. The vertical dashed green and dotted red lines are at values of λ_k/λ_0 equal to 0.33 and 0.1, respectively.

Similarly, in the frame of reference of the magnetic structure, if we define $L = 0$ as the L position of the X line, then B_n should change sign across $L = 0$. So one might think that the B_n-dependent terms in Equation 4 would make the greatest contribution to $V_{str,l}$. But B_n is small (Figure 2e), and the greatest contributions to $V_{str,l}$ come from the B_m and B_l-dependent terms in Equation 4 (green and blue curves in Figure 4c, respectively).

The magnitude of $V_{str,i}$, where $i = L$ or N, can be found from the magnitudes of $V_{str,k}$, where $k = l$, m, or n, using

$$V_{str,i} = \sqrt{\cos^2\left(\theta_{i,n}\right)V_{str,n}^2 + \cos^2\left(\theta_{i,l}\right)V_{str,l}^2 + \cos^2\left(\theta_{i,m}\right)V_{str,m}^2}, \quad (10)$$

where $\theta_{i,k}$ is the angle between the i (L or N) and k (l, m, or n) directions. Figure 4e shows $\cos^2\theta_{i,m}$ for $i = L$ (blue curve) and $i = N$ (red curve). Because these values are small, especially for $i = N$, the neglect of $V_{str,m}$ in the calculation of $V_{str,N}$ leads to almost no inaccuracy, and the neglect of $V_{str,m}$ in the calculation of $V_{str,L}$ is not a significant problem unless $V_{str,m} \gg V_{str,l}$. But Figure 3 shows that $V_{str,m}$ (green dots) does not become much greater than $V_{str,l}$ unless the minimum eigenvalue λ_{min} becomes very small ($<0.1\lambda_0$), for which $V_{str,m}$ is not expected to be accurate. Therefore, our STD values of $V_{str,N}$ should be very accurate, and despite the fact that λ_{int} in Figure 2a (blue curve) is not always above our desired value for accuracy (dotted black line), there are indications that $V_{str,L}$ may be accurate. These include the fact that neither the maximum or intermediate gradient components of $V_{str,k}$ increase with decreasing eigenvalue in Figure 3, and the comparison with the velocity calculated from reconstruction described below.

3.3. Polynomial Reconstruction

Figure 5 shows that the RQ-3D polynomial model well represents **B** and **J** during the time interval t = 1.6 –2.8 s. The J_N component is not as well modeled as the other components, but it is very small compared to the other components of **J**. This shows that the model is reasonable in the vicinity of the spacecraft, though it does not necessarily show that the model is accurate away from the spacecraft.

Figure 6 shows reconstruction results for the magnetic field in the L–N plane at $M = 0$, where here L, M, and N are measured with respect to the centroid of the MMS spacecraft, at the origin in Figures 6b–6q. The reconstruction appears to show a reconnection X line (extending normal to the L–N plane, so that it is an X point in that plane), indicated by the gold asterisk, that appears slightly after t = 1.6 s. The X line does not move much until about t = 1.92 s. Then between t = 1.92 and 2.24 s it moves rapidly in the minus L direction relative to the spacecraft. Later, it reappears near the left (negative L) side of the plot from t = 2.4 –2.8 s. While the L position of the X line is somewhat variable, the X line appears to move uniformly in the minus N direction relative to the spacecraft. Movie S1 in the Supplementary Information shows the time dependence of the reconstruction in more detail.

3.4. Path of the Spacecraft Through the Magnetic Structure

Figures 7a and 7b show the motion of the reconnection X line relative to the centroid of the MMS spacecraft in the L and N directions, respectively, based on the RQ-3D polynomial reconstruction using data such as in Figure 6. At each time, the position in the L-N plane is found where the in-plane magnetic field is a minimum (indicated by the gold asterisks in Figures 6b–6q) (There are also minima corresponding to reconnection O points, but these have been removed from Figure 7).

The red curve in Figure 7c makes use of the positions from Figures 7a and 7b to show the path of the centroid of the MMS spacecraft relative to the X line, which is at the origin of Figure 7c. The L_{MMS} and N_{MMS} components in Figure 7c have been converted to km using d_{sc} = 18.3 km. The path progresses generally

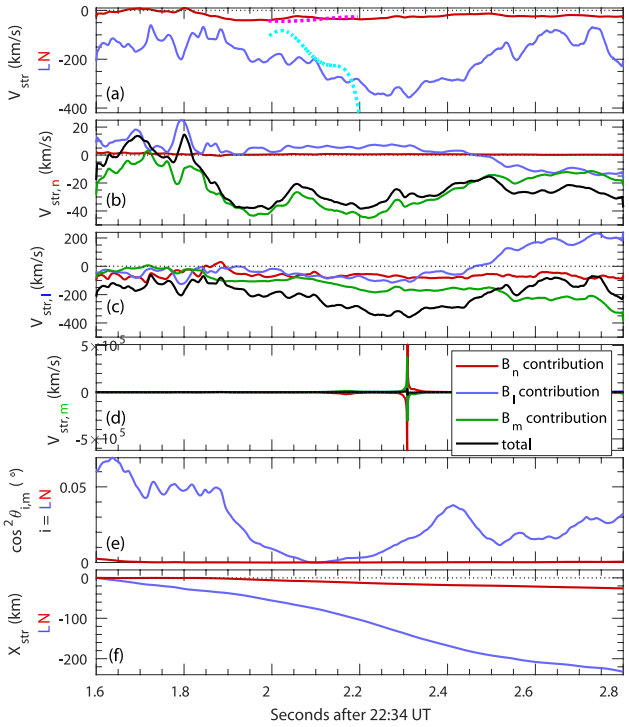

Figure 4. Spatial-Temporal Difference (STD) results. (a) STD velocity components in the L (blue solid curve) and N (red solid curve) directions calculated using only contributions from the MDD local n and l directions (b–d) STD velocity component in the MDD local (b) n, (c) l, and (d) m directions, where the black curve is the total component $V_{str,k}$ for $k = n$, l, or m, and the red, blue, and green curves are the contributions to $V_{str,k}$ from the B_n, B_l, and B_m terms in Equation 4, respectively; (e) squared cosine of the angle between the L (blue curve) or N (red curve) direction and the m direction; (f) net STD displacement from $t = 1.6$ s in the L (blue curve) and N (red curve) directions. The dotted curves in Figure 4a are the L (cyan curve) and N (magenta curve) velocity components found from RQ-3D reconstruction during the time when the centroid of the MMS spacecraft was within two average spacecraft separations, d_{sc}, from the X line of the magnetic structure.

from the left to the right, starting at the black circle. There are some reversals with respect to time of the velocity in the L direction, v_L, at positions indicated by the black arrows. At these positions, all outside a radius of 2 spacecraft spacings (2 d_{sc}) as indicated by the solid green curve, the reconnection X line seems to linger near the periphery of the reconstruction (at a distance of about 2–3 d_{sc}).

The blue curve shows the path of the MMS spacecraft found from STD. The magenta circle at the left side of the plot shows the starting point of the path. While the STD path is shown for the entire time interval of Figures 7a and 7b, 1.6 –2.9 s, the points plotted within the red curve are only for the times when L_X and N_X determined from the reconstruction are within $\pm 3 d_{sc}$, that is, the times for which there are blue data points shown in Figures 7a and 7b.

The STD method yields only velocities, not positions, so the position of the path is determined in the following way. For an X-like reconnection configuration at $(L, N) = (0,0)$, B_N is expected to change sign with respect to L at $L = 0$, and B_L is expected to change sign with respect to N at $N = 0$. So the path is adjusted in the left to right direction so that the N component of the magnetic field averaged over the four spacecraft reverses at $L_{MMS} = 0$ (red curve in Figure 2e at $t = 2.12$ s). This exact procedure cannot be followed to determine the vertical position of the path using B_L, because $B_{L,av}$ does not reverse during our time interval (green curve in Figure 2e), indicating that the centroid of the spacecraft positions did not cross the N axis, as depicted in Figure 7c (blue curve). But MMS3 is displaced 10.1 km in the positive N direction relative to the centroid of the MMS spacecraft (See the positions of the green circles in Figures 6b–6q relative to the origin at the centroid of the spacecraft). And MMS3 did cross the $N = 0$ line, as indicated by a reversal in B_L at 2.81 s (green curve in Figure 5a just beyond the right side of the plot). At this time the centroid of the MMS positions was at the large red circle on the right side of Figure 7c. The STD path was adjusted in the up to down direction by requiring that $N_{MMS} = 0$ was 10.1 km above the red circle.

The path of the MMS spacecraft from the reconstruction (red curve) is mostly consistent with that from STD within a distance of 2 d_{sc} from the X line (within the solid green circle). That is, with a slight shift of the blue curve downward, the two curves would almost exactly lie on top of each other for those parts of the curves that would be within the solid green circle. During the time that the centroid of the MMS spacecraft is within $2d_{sc}$ of the X line (1.99 –2.20 s, indicated by the vertical solid green lines in Figures 7a and 7b), the L and N components of the velocity based on the reconstruction were 180 and 32 km/s, respectively, whereas the L and N components of the velocity based on the STD method were 236 and 32 km/s, respectively. So the N components of the velocity were the same for both methods, and the L components agreed within no more than 30% (depending on how we calculate the percent difference).

Note also that both STD and the reconstruction show the largest L component of the structure velocity at about $t = 2.23$ s (based on the solid blue curve in Figure 4a and the blue curve in Figure 7a). A more precise comparison is shown in Figure 4a, where the dotted curves are the L component (cyan dotted curve) and N component (magenta dotted curve) of the structure velocity based on the motion of the X line in the polynomial reconstruction. The N components from the reconstruction is quite similar to that from STD (comparing the red solid and magenta dotted curves in Figure 4a), especially at $t = 2.0$ s and between 2.1 and 2.2 s. There are larger differences for the L component (comparing the blue solid and cyan dotted curves in Figure 4a), but both methods yield increasingly negative velocities with respect to time, and the average values are similar.

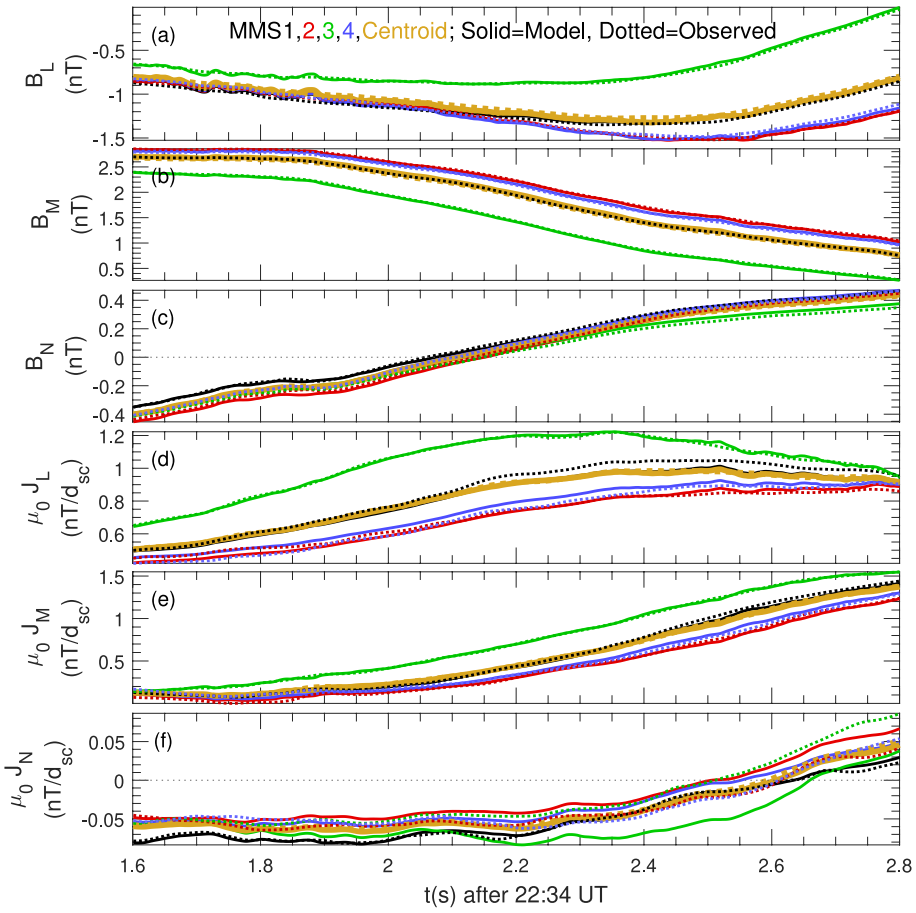

Figure 5. Model and observed magnetic field and current density. (a–c) observed (dotted curves) and RQ-3D model (solid curves) *L*, *M*, and *N* components of **B** for the individual Magnetospheric Multiscale (MMS) spacecraft, using the colors in the key of panel a; and (d–f) the particle current density **J** using the same colors and line styles as for **B**. The gold curves are the average of the observed values (dotted curves) and the model values at the centroid of the spacecraft positions (solid curves).

4. Discussion

We have explained aspects of the STD method of Shi et al. (2006, 2019), and have shown how STD and the polynomial reconstruction method of Denton et al. (2020) can be used to determine the velocity of the magnetic structure relative to the MMS spacecraft, and then the path of the MMS spacecraft relative to the X line of the magnetic structure (Figure 7c). In order to get the path from the STD method, we had to use the time of reversal in B_N averaged over the MMS spacecraft to align the path in the *L* direction, and the time of reversal in B_L as observed by MMS3 to align the path in the *N* direction. Because the latter event occurred significantly later in time than the closest approach to the X line (2.814 s; see position of the red circle in Figure 7c), the position of the STD path probably has more uncertainty in the *N* direction than in the *L* direction. So it would not be unreasonable to shift the path from STD (blue curve in Figure 7c) slightly down to align it with the path from the reconstruction (red curve in Figure 7c). The two paths would then agree quite well for the time for which the centroid of the MMS spacecraft is within $2d_{sc}$ from the X line (within the solid green circle of Figure 7c).

The reconstruction is more likely to be accurate when the centroid of the MMS spacecraft is close to the X line, but the path calculated from STD has no such restriction. The STD and reconstruction paths agree when the centroid of the spacecraft are within a distance of $2d_{sc}$ from the X line, roughly validating both methods when the MMS spacecraft are close to the X line. Calculating the velocity of the MMS spacecraft relative to the X line based on these two methods during the interval of time that the centroid of the

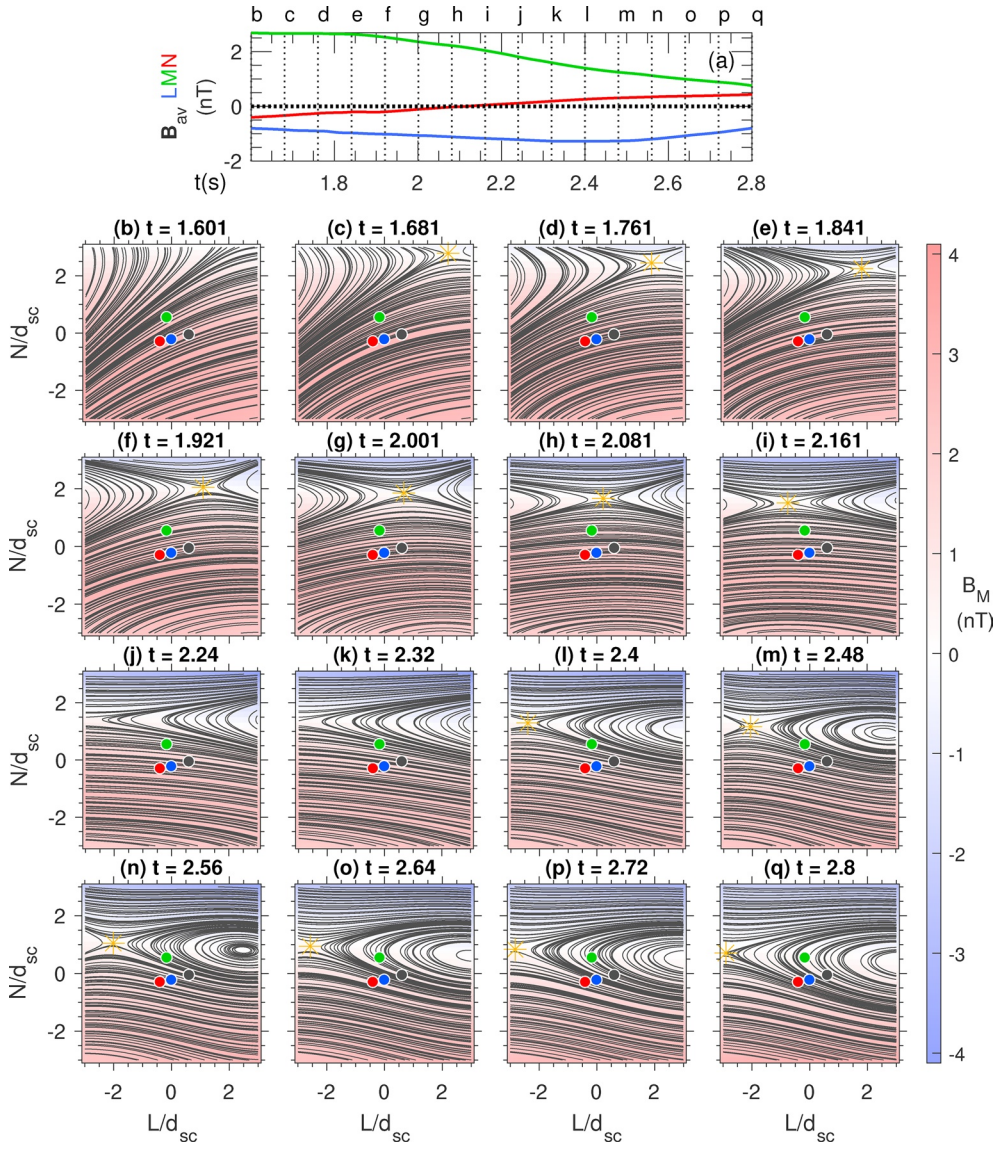

Figure 6. RQ-3D reconstruction of the magnetic field in the L–N plane at $M = 0$. (a) The magnetic field averaged over the spacecraft, $\mathbf{B}_{av}$; and (b–q) streamlines of the in-plane magnetic field at $M = 0$ (black curves) and B_M (color) for B_M directed into the page using the color scale at the right side of the plot. Each plot is generated at the time indicated in the panel label corresponding to the time of the same label in panel (a) The coordinates L and N are measured relative to the centroid of the MMS spacecraft (at the origin of each panel), and the positions of the MMS spacecraft are indicated by the colored circles for MMS1 (black circle), MMS2 (red circle), MMS3 (green circle), and MMS4 (blue circle). The gold asterisks are the position of the X line determined from the in-plane magnetic field minimum.

spacecraft was within a distance of $2d_{sc}$ from the X line based on the reconstruction, we found that the N component of the velocity from STD and the reconstruction agreed precisely, while the L components agreed to within no more than 30%. But there is no reason that the STD results should be less accurate when the MMS spacecraft are not close to the X line. So we conclude that the position of the X line from the reconstruction is only likely to be accurate when the centroid of the MMS spacecraft is within $2d_{sc}$ from the X line, and the STD velocity is likely to be more accurate than the reconstruction velocity when the MMS spacecraft are farther away from the X line.

As mentioned in Section 3.1, Genestreti et al. (2018) found L, M, and N directions (their MDD-B/MVA-v_e coordinate system, coordinate system 14 in their Table A1) that varied by 40°, 39°, and 11°, respectively, from our directions. Their analysis used MDD to get the N direction, but the maximum variance direction

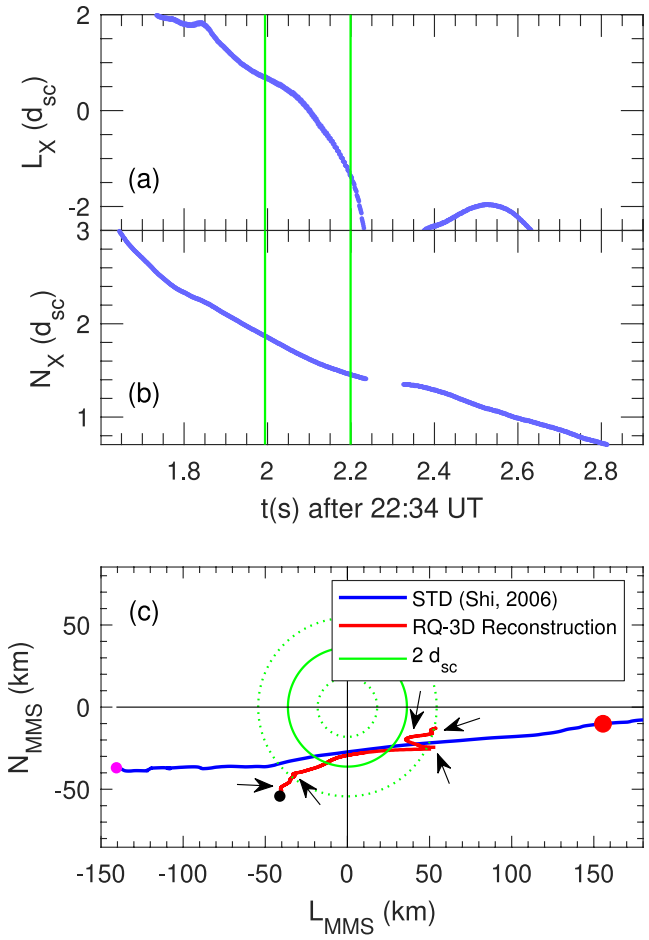

Figure 7. Motion of the spacecraft in the *L*-*N* plane. (a–b) *L* and *N* coordinates of the X line relative to the centroid of the MMS spacecraft from the RQ-3D reconstruction, (a) L_X and (b) N_X, respectively, in units of the average spacecraft spacing, d_{sc}, versus time *t*. (c) Path of the centroid of the MMS spacecraft through the *L*-*N* plane relative to the X line at the origin. The blue curve is from the Spatio-Temporal Difference (STD) method, and the red curve is from the reconstruction. Both paths start toward the left side of the plot and progress generally toward the right side. The black circle marks the starting point of the reconstruction path, and the black arrows represent positions along that path where there is a reversal of the *L* component of the velocity, v_L. The magenta circle marks the starting point of the STD path. The solid green circle is at $2d_{sc}$ from the origin.

of the electron velocity to get the *L* direction. They were strongly motivated by the goal of finding an *M* direction that yielded constant E_M. The constancy of E_M follows from Faraday's Law if the reconnection is two-dimensional (in the *L*–*N* plane) and time independent. In other words, this coordinate system was also motivated by the goal of determining *M* as the direction of invariance of the magnetic field. To avoid confusion with the directions based on MDD, we will indicate these directions by a "G" subscript. Unfortunately, we are not able to accurately calculate the velocity in the L_G–N_G plane using STD, because the velocity in the L_G direction would have a significant contribution from the velocity in our *M* direction. Then, because the gradient in our *M* direction is very small, the velocity in the L_G direction cannot be reliably determined. Nevertheless, we project our STD velocity onto the L_G and N_G directions to get what is probably a lower limit on these velocity components.

We also determine the velocity in the L_G–N_G plane using an RQ-3D reconstruction. Figure 8 shows the reconstructed magnetic field using the same format as Figure 6. In Figure 8, the X line moves across the field of view from right to left, as in Figure 6, but does not linger at the periphery of the plot where $L_G/d_{sc} = \pm 3$. Figure 9 is similar to Figure 7, but showing the motion of the spacecraft with respect to the L_G and N_G coordinates. The dashed blue curve in Figure 9 shows the path calculated from STD including all velocity components with eigenvalues to the right of the dotted vertical red line in Figure 3. Thus a small number of *m* velocity component values are included in the calculation of the L_G and N_G components of the STD velocity. The fact that the dashed blue curve in Figure 9 is slightly closer to the red curve than the blue curve is suggestive that inclusion of the missing *m* component of velocity might possibly lead to better agreement between STD and the polynomial reconstruction.

Figure 10 compares velocity components in the L_G and N_G directions that we calculate to those that have appeared in several other references listed in Table 1. First of all, we use four spacecraft timing analysis using B_{M_G} and J_{M_G} to determine the N_G components of the velocity only (Dunlop & Woodward, 1998). The angle between the timing normal and the Genestreti et al (2018). N_G direction, θ_N, is small in both cases, as shown in Table 1. Therefore, the timing analysis is approximately giving the velocity in the *N* direction. But the results differ greatly depending on the quantity used, as indicated by −122 km/s value found using B_{M_G} and the −40 km/s value found using J_{M_G} (see the red horizontal lines in Figure 10). The velocity found from projection of our STD velocity onto the L_G and N_G directions is indicated in Table 1 and Figure 10 by the "S" symbol (red in Figure 10), and for the reconstruction using the "R" symbol (red in Figure 10). Velocities from Nakamura et al. (2019), Hasegawa et al. (2019), and Egedal et al. (2019) are indicated in Table 1 and Figure 10 respectively by the "N," "H," and "E" symbols (blue in Figure 10).

The N_G components from STD and RQ-3D and the three studies referenced are fairly consistent (letter symbols in Figure 10), and lie between the values from the timing analysis (red horizontal lines in Figure 10). The L_G velocity component from STD is significantly less in magnitude than the other estimates, probably owing to the problem of evaluating the STD velocity component in the M_G direction, mentioned previously. The L_G velocity component from the reconstruction is equal to that from the Egedal et al. (2019) reference, and this estimate has the largest magnitude.

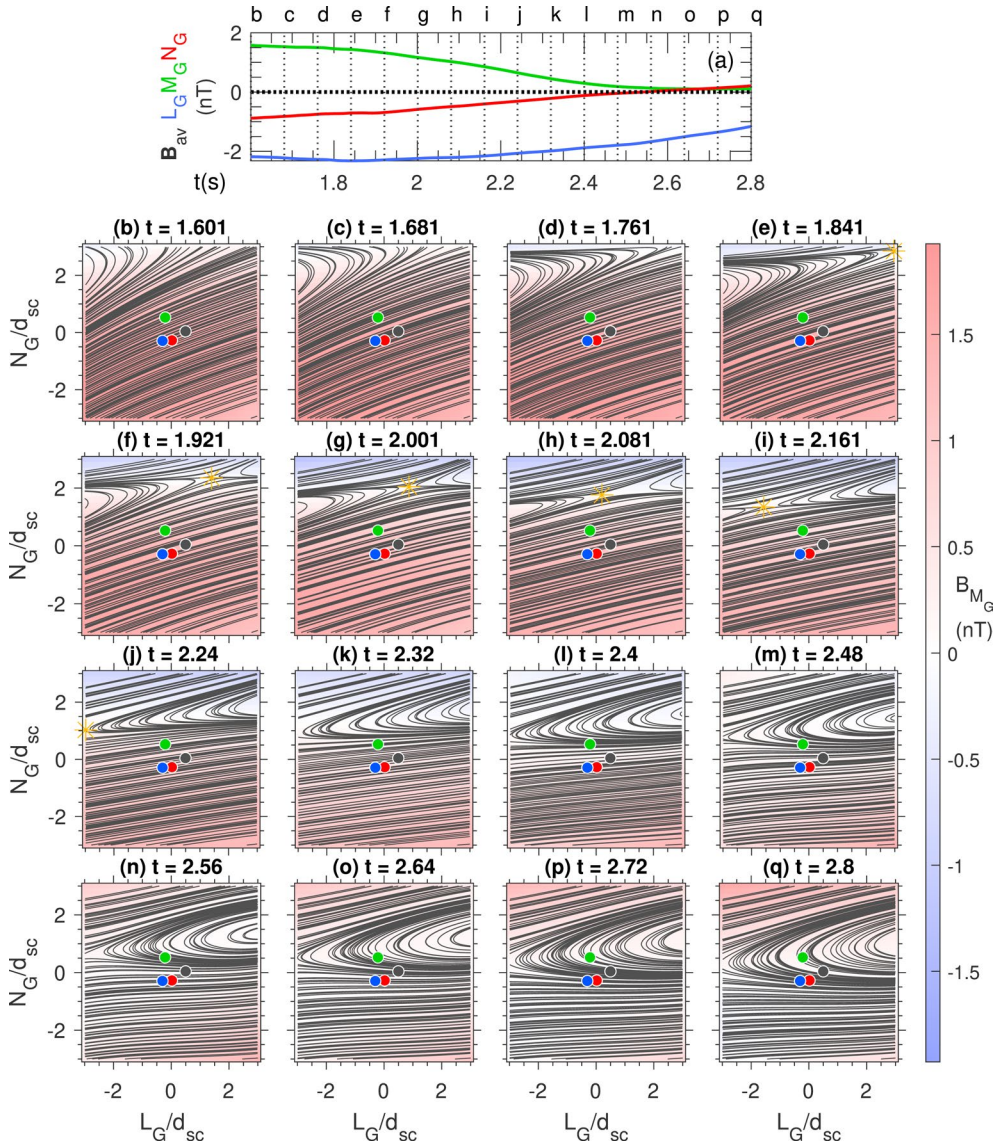

Figure 8. RQ-3D reconstruction of the magnetic field in the L_G–N_G plane at $M_G = 0$. Same as Figure 6, except showing the magnetic field in the L_G–N_G rather than L–N plane.

In the *L*-*N* coordinate system based on MDD analysis, the STD and reconstruction velocities agree fairly well (within about 30%), at least when the centroid of the MMS spacecraft is within $2d_{sc}$ of the X line. This would appear to roughly validate both of these methods ("roughly" because the *L* components of the velocities in Figure 4a are certainly not exactly the same). Also, the *L* coordinate in Figure 6 based on MDD seems to be much better aligned with the current sheet than that in Figure 8.

There are some differences in results with different data processing. If we do not make any adjustment of the electron current density (Section 2.1), the reconstruction yields some additional time-dependent behavior (as shown in Movie S2 in the Supplementary Information). There appears to be coalescence-like merging of a plasmoid with the large scale island. Because the merging plasmoid is elongated in the *L* direction, this process would not be energetically favorable; so we do not regard this short timescale behavior to be realistic. Furthermore, electron magnetohydrodynamic (EMHD) reconstructions of the July 11, 2017 event for each of the four MMS spacecraft (shown in the Supplementary Information of Hasegawa et al. (2019)) did not reconstruct any plasmoid structures, so the reconstruction results are more consistent with the adjustment of the electron density. If the electron density is adjusted as described in Section 2.1, but the

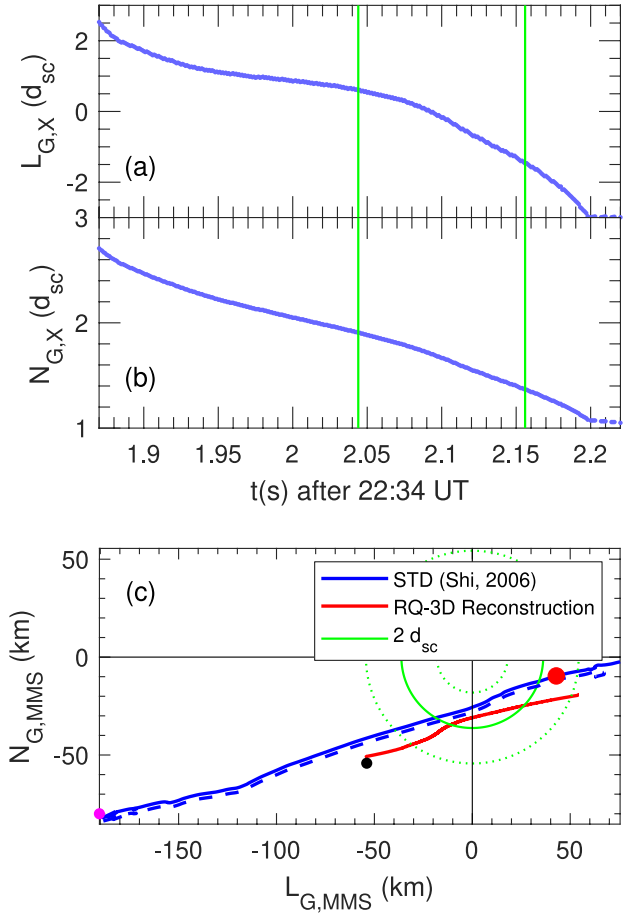

Figure 9. Motion of the spacecraft in the L_G–N_G plane. Similar to Figure 7, except showing the motion using the L_G and N_G rather than L and N coordinates. The blue dashed curve in Figure 8c is found from STD making use of all velocity components to the right of the red vertical dotted line in Figure 3.

data are smoothed over 0.3 s rather than 0.5 s, the reconstructions are similar to those without the density adjustment (as shown in Movie S3 in the Supplementary Information). An elongated plasmoid merges into the magnetic island in such a way that appears to be unrealistic. With smoothing of 1.0 s, the velocities are not surprisingly more constant, but there is less agreement between the velocities from STD and the reconstruction (reconstruction L component 35% lower in magnitude than the STD L component). We repeat the results of this study for 1.0 s smoothing in the Supplementary Information (Movie S4 and Text S2).

Our L-M-N coordinate system based on MDD is best for comparing the results for velocity from STD and the reconstruction, because STD cannot reliably determine the component of the velocity in the minimum gradient (M) direction. Genestreti et al. (2018), however, argued that relatively small magnetic field calibration errors could significantly alter the MDD directions. In particular, their Figure 8 suggests that calibration errors for **B** of order 0.05 nT can cause errors in the L and M directions with typical values of 10°, but ranging from small values to 20°. There is definitely an inconsistency between the M component directions based on the minimum gradient from MDD or the constancy of E_M, used to validate Genestreti et al.'s coordinate system. This is because the argument that E_M should be constant is based on supposed invariance of **B** in the M direction, which should be the MDD minimum gradient direction. Genestreti and coworkers looked for coordinate systems for which the small value E_M was not dependent on the larger E_N. They found that E_M in the MDD coordinate system varied with E_N, and on average was negative, implying that reconnection would not be occurring. On the other hand, $E_{M,G}$ was relatively independent of $E_{N,G}$.

Other results favoring a coordinate system similar to that of Genestreti and coworkers are the optimal coordinate system for Electron MHD (EMHD) reconstruction (Hasegawa et al., 2019) and the good correlation between **B** and the electron velocity as the magnetic field rotates from the L to M direction (Le et al., 2010) found in the simulation of this event by Egedal et al. (2019). This rotation is consistent with the wave reconnection dynamics first described by Mandt et al. (1994), and then later generalized to electron scale structures (Le et al., 2010, 2013). Another argument favoring the Genestreti and coworkers coordinate system is that the L_G component of the electron velocity shows a reversal when the spacecraft passed near the X line in the L_G direction, whereas the L component of the electron velocity in our MDD coordinate system has a single peak, similar to that of the M component.

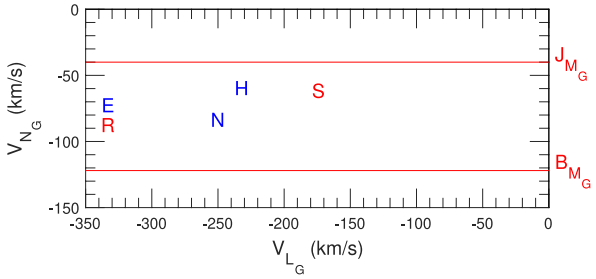

Figure 10. Magnetic structure velocities in the L_G-N_G plane. Velocities calculated in this study (red symbols) along with velocities in various references (blue symbols), using the symbols listed in Table 1.

Of course, evaluating the coordinate system based on the constancy of E_M also involves assumptions, two dimensionality, no time dependence, and accurate calculation of the electric field. But we cannot rule out the possibility that magnetic field calibration errors are affecting the inferred magnetic structure (like the orientation of the current sheet in Figure 6) and our results for $V_{str,L}$. For that reason, we also calculated the reconstruction velocity in Genestreti and coworker's coordinate system. The gradient in the N direction, and hence $V_{str,N}$, however, is much better determined than that in the L direction, and at any rate, the N directions of both coordinate systems were fairly similar, differing by 11°.

Even if the minimum magnetic field gradient direction was determined correctly, results by Denton et al. (2016a, 2018) indicate that the minimum gradient direction can be the L direction determined to have

Table 1
Magnetic Structure Velocities in the Genestreti et al. (2018) L_G–N_G Plane

Symbol in Figure 6	θ_L[a] (°)	V_{L_G} (km/s)	θ_N[b] (°)	V_{N_G} (km/s)	References
B_{M_G}	–	–	3.7	−122	This study, timing with B_{M_G}
J_{M_G}	–	–	11.5	−40	This study, timing with J_{M_G}
S	0	−174	0	−61	This study, STD
R	0	−333	0	−87	This study, RQ-3D reconstruction
N	0	−250	0	−83	Nakamura et al. (2019)
H	5.0	−232	0.6	−59	Hasegawa et al. (2019)
E	10.6	−333	6.5	−72	Egedal et al. (2019)

[a]Angle between the L_G and reference L directions. [b]Angle between the N_G and reference N directions.

maximum variation in the magnetic field, which we usually associate with the reconnection magnetic field. Perhaps some sort of reconciliation for the difference in the M direction based on the magnetic field gradient or constancy in the electric field results from the fact that the magnetic field geometry is in some sense approximately one dimensional based on the relative size of the maximum and intermediate gradient eigenvalues in Figure 2a. From that perspective, there are two directions of relatively small spatial inhomogeneity relative to that of the N direction. At any rate, it seems that different kinds of data align themselves better to different coordinate systems.

Because the STD and reconstruction velocities are not exactly the same, and because the reconstruction results differ somewhat depending on the data processing, the methods as implemented here must be regarded as only providing a rough estimate of the magnetic structure velocity. But both STD and the reconstruction would work better if the spacecraft spacing were somewhat larger, so that the gradients would be better determined and λ_k would be larger relative to λ_0 (The spacing should be not so much larger that the spacecraft are sampling different structures). Both the STD and reconstruction results strongly depend on the observed gradients in the magnetic field components. It is encouraging, however, that for this event the STD L component of the velocity was affected most strongly by the variation of B_M and B_L, and less so (though not insignificantly) by the variation of B_N (Figure 4b), whereas the L component of the velocity from the polynomial reconstruction was affected mostly by the spatial variation in B_N (since the X line was at the reversal in B_N). Also our estimate for $\mathbf{V}_{\rm str}$ in the Genestreti et al. (2018) coordinate system based on the reconstruction did not differ greatly from other velocity estimates (Figure 10).

Appendix A: Derivation of STD Structure Velocity

Expressing (2) as a matrix equation,

$$\mathbf{B}_{dt} = -\mathbf{V}_{\rm str} \cdot \mathbf{G}, \tag{A1}$$

where $\mathbf{B}_{dt}$ and $\mathbf{V}_{\rm str}$ are row vectors, and

$$\mathbf{G} = \nabla \mathbf{B} \tag{A2}$$

is a matrix with the partial spatial derivatives varying along the column direction.

Now we multiply (A1) by the transpose of $\mathbf{G}$, $\mathbf{G}^T$, to get

$$\mathbf{B}_{dt} \cdot \mathbf{G}^T = -\mathbf{V}_{\rm str} \cdot \mathbf{G} \cdot \mathbf{G}^T = -\mathbf{V}_{\rm str} \cdot \mathbf{M}_{\rm G}, \tag{A3}$$

where

$$\mathbf{M}_{\rm G} = \mathbf{G} \cdot \mathbf{G}^T. \tag{A4}$$

Assume that we have used MDD to get the local time-dependent gradient directions, n, l, and m. At each time, we define a rotation matrix, $\mathbf{M}$, that has the eigenvectors along the columns.

Now we transform to the local eigenvector frame by multiplying (A3) by $\mathbf{M}$ on the right and using $\mathbf{M}\cdot\mathbf{M}^T = I$, where I is the identity matrix, to get

$$\mathbf{B}_{dt}\cdot\mathbf{M}\cdot\mathbf{M}^T\cdot\mathbf{G}^T\cdot\mathbf{M} = -\mathbf{V}_{\mathrm{str}}\cdot\mathbf{M}\cdot\mathbf{M}^T\cdot\mathbf{M}_{\mathrm{G}}\cdot\mathbf{M}, \tag{A5}$$

or

$$\mathbf{B}_{dt}\cdot\mathbf{G}^T = -\boldsymbol{\mathcal{V}}_{\mathrm{str}}\cdot\boldsymbol{\mathcal{M}}_{\mathrm{G}}. \tag{A6}$$

Then, as described by Shi et al. (2006), we can solve for $\mathcal{V}_{\mathrm{str}}$ in closed form (Equation 3) using the fact that $\mathcal{M}_G$ is diagonal in the local MDD coordinate system l-m-n with the gradient eigenvalues, λ_k.

Appendix B: Model Current Density

To calculate the current density $\mu_0\mathbf{J}$ for the Reduced Quadratic model of Denton et al. (2020), we simply take the curl of Equations 6–8. For instance, $\mu_0 J_l = \partial B_n/\partial m - \partial B_m/\partial n$. The result is:

$$\mu_0 J_l = \frac{\partial B_n}{\partial m} - \left(\frac{\partial B_m}{\partial n} + \frac{\partial^2 B_m}{\partial n^2}n + \frac{\partial^2 B_m}{\partial n \partial l}l\right) \tag{B1}$$

$$\mu_0 J_m = \frac{\partial B_l}{\partial n} + \frac{\partial^2 B_l}{\partial n^2}n - \left(\frac{\partial B_n}{\partial l} + \frac{\partial^2 B_n}{\partial l^2}l\right) \tag{B2}$$

$$\mu_0 J_n = \frac{\partial B_m}{\partial l} + \frac{\partial^2 B_m}{\partial n \partial l}n + \frac{\partial^2 B_m}{\partial l^2}l - \frac{\partial B_l}{\partial m} \tag{B3}$$

Note that $\mu_0\mathbf{J}$ is at most linear with respect to l and n since the curl operation involves a derivative.

Data Availability Statement

The MMS data set is available on-line at https://lasp.colorado.edu/mms/sdc/public/links/.

Acknowledgments
Work at Dartmouth College was supported by NASA grant 80NSSC19K0254. The French LPP involvement for the SCM instrument is supported by CNES and CNRS.

References

Alm, L., Argall, M. R., Torbert, R. B., Farrugia, C. J., Burch, J. L., Ergun, R. E., et al. (2017). EDR signatures observed by MMS in the 16 October event presented in a 2-D parametric space. *Journal of Geophysical Research: Space Physics*, *122*(3), 3262–3276. https://doi.org/10.1002/2016ja023788

Argall, M. R., Fischer, D., Le Contel, O., Mirioni, L., Torbert, R. B., Dors, I., et al. (2018). *The fluxgate-searchcoil merged (FSM) magnetic field data product for MMS*. ArXiv. https://arxiv.org/abs/1809.07388

Burch, J. L., Moore, T. E., Torbert, R. B., & Giles, B. L. (2015). Magnetospheric Multiscale overview and science objectives. *Space Science Reviews*, *199*, 5–21. https://doi.org/10.1007/s11214-015-0164-9

Denton, R. E., Sonnerup, B. U. O., Hasegawa, H., Phan, T. D., Russell, C. T., Strangeway, R. J., et al. (2016a). Motion of the MMS spacecraft relative to the magnetic reconnection structure observed on 16 October 2015 at 1307 UT. *Geophysical Research Letters*, *43*(11), 5589–5596. https://doi.org/10.1002/2016gl069214

Denton, R. E., Sonnerup, B. U. O., Hasegawa, H., Phan, T. D., Russell, C. T., Strangeway, R. J., et al. (2016b). Reconnection guide field and quadrupolar structure observed by MMS on 16 October 2015 at 1307 UT. *Journal of Geophysical Research: Space Physics*, *121*, 9880–9887. https://doi.org/10.1002/2016ja023323

Denton, R. E., Sonnerup, B. U. O., Russell, C. T., Hasegawa, H., Phan, T. D., Strangeway, R. J., et al. (2018). Determining L-M-N current sheet coordinates at the magnetopause from Magnetospheric Multiscale data. *Journal of Geophysical Research*, *123*, 2274–2295. https://doi.org/10.1002/2017ja024619

Denton, R. E., Torbert, R. B., Hasegawa, H., Dors, I., Genestreti, K. J., Argall, M. R., et al. (2020). Polynomial reconstruction of the reconnection magnetic field observed by multiple spacecraft. *Journal of Geophysical Research: Space Physics*, *125*, e0027JA027481. https://doi.org/10.1029/0027JA027481

Dunlop, M. W., & Woodward, T. I. (1998). Multi-spacecraft discontinuity analysis: Orientation and motion. In G. Paschmann, & P. Daly (Eds.), *Analysis methods for multi-spacecraft data* (pp. 271–306). Switzerland: International Space Science Institute, SR-001.

Egedal, J., Ng, J., Le, A., Daughton, W., Wetherton, B., Dorelli, J., et al. (2019), Pressure tensor elements breaking the frozen-in law during reconnection in earth's magnetotail, *Physical Review Letters*, *123*(22).https://doi.org/10.1103/PhysRevLett.123.225101

Fischer, D., Magnes, W., Hagen, C., Dors, I., Chutter, M. W., Needell, J., et al. (2016). Optimized merging of search coil and fluxgate data for MMS. *Geoscientific Instrumentation Methods and Data Systems Discussions*, *5*(2), 521–530. https://doi.org/10.5194/gi-5-521-2016

Genestreti, K. J., Nakamura, T. K. M., Nakamura, R., Denton, R. E., Torbert, R. B., Burch, J. L., et al. (2018). How accurately can we measure the reconnection rate *E*−*M* for the MMS diffusion region event of 11 July 2017? *Journal of Geophysical Research: Space Physics*, *123*, 9130–9149. https://doi.org/10.1029/2018ja025711

Hasegawa, H., Denton, R. E., Nakamura, R., Genestreti, K. J., Nakamura, T. K. M., Hwang, K. J., et al. (0027). Reconstruction of the electron diffusion region of magnetotail reconnection seen by the MMS spacecraft on 11 July 2017. *Journal of Geophysical Research: Space Physics*, *124*, 122–138. https://doi.org/10.1029/2018ja026051

Hesse, M., Aunai, N., Birn, J., Cassak, P., Denton, R. E., Drake, J. F., et al. (2014). Theory and modeling for the Magnetospheric Multiscale mission. *Space Science Reviews*. *199*, 577–630. https://doi.org/10.1007/s11214-014-0078-y

Hesse, M., Neukirch, T., Schindler, K., Kuznetsova, M., & Zenitani, S. (2011). The diffusion region in collisionless magnetic reconnection. *Space Science Reviews*, *160*(1–4), 3–23. https://doi.org/10.1007/s11214-010-9740-1

Le, A., Egedal, J., Fox, W., Katz, N., Vrublevskis, A., Daughton, W., & Drake, J. F. (2010). Equations of state in collisionless magnetic reconnection. *Physics of Plasmas*, *17*(5). https://doi.org/10.1063/1.3309425

Le, A., Egedal, J., Ohia, O., Daughton, W., Karimabadi, H., & Lukin, V. S. (2013). Regimes of the electron diffusion region in magnetic reconnection. *Physical Review Letters*, *110*(13). https://doi.org/10.1103/PhysRevLett.110.135004

Le Contel, O., Leroy, P., Roux, A., Coillot, C., Alison, D., Bouabdellah, A., et al. (2016). The search-coil magnetometer for MMS. *Space Science Reviews*, *199*(1–4), 257–282. https://doi.org/10.1007/s11214-014-0096-9

Mandt, M. E., Denton, R. E., & Drake, J. F. (1994). Transition to whistler mediated magnetic reconnection. *Geophysical Research Letters*, *21*(1), 73–76. https://doi.org/10.1029/93gl03382

Manuzzo, R., Belmont, G., Rezeau, L., Califano, F., & Denton, R. E. (2019). Crossing of plasma structures by spacecraft: A path calculator. *Journal of Geophysical Research: Space Physics*, *124*(12), 10119–10140. https://doi.org/10.1029/0027JA026632

Nakamura, R., Genestreti, K. J., Naltamora, T., Baumjohann, W., Varsani, A., Nagai, T., et al. (2019). Structure of the current sheet in the 11 July 2017 Electron Diffusion Region event. *Journal of Geophysical Research: Space Physics*, *124*(2), 1173–1186. https://doi.org/10.1029/2018JA026028

Pollock, C., Moore, T., Jacques, A., Burch, J., Gliese, U., Saito, Y., et al. (2016). Fast plasma investigation for Magnetospheric Multiscale. *Space Science Reviews*, *199*, 331–406. https://doi.org/10.1007/s11214-016-0245-4

Robert, P., Dunlop, M. W., Roux, A., & Chanteur, G. (1998). Accuracy of current density determination. In G. Paschmann, & P. Daly (Eds.), *Analysis methods for multi-spacecraft data* (pp. 395–418). Switzerland: International Space Science Institute, SR-001.

Russell, C. T., Anderson, B. J., Baumjohann, W., Bromund, K. R., Dearborn, D., Fischer, D., et al. (2016). The Magnetospheric Multiscale magnetometers. *Space Science Reviews*, *199*, 189–256. https://doi.org/10.1007/s11214-014-0057-3

Shi, Q. Q., Pu, Z. Y., Zhang, H., Fu, S. Y., Xiao, C. J., Zong, Q. G., et al. (2005). Simulation studies of high-latitude magnetospheric boundary dynamics. *Surveys in Geophysics*, *26*(1–3), 369–386. https://doi.org/10.1007/s10712-005-1900-6

Shi, Q. Q., Shen, C., Dunlop, M. W., Pu, Z. Y., Zong, Q. G., Liu, Z. X., et al. (2006). Motion of observed structures calculated from multi-point magnetic field measurements: Application to Cluster. *Geophysical Research Letters*, *33*, L08109. https://doi.org/10.1029/2005gl025073

Shi, Q. Q., Tian, A. M., Bai, S. C., Hasegawa, H., Degeling, A. W., Pu, Z. Y., et al. (2019). Dimensionality, coordinate system and reference frame for analysis of in-situ space plasma and field data. *Space Science Reviews*, *215*(4). https://doi.org/10.1007/s11214-019-0601-2

Sonnerup, B. O. U. (1979). Magnetic field reconnection. In *Solar system plasma physics* (Vol. *3*, A79–53667 24–46, pp. 45–108). Amsterdam: North-Holland Publishing Co.

Sonnerup, B. U., & Cahill, L. J. (1967). Magnetopause structure and attitude from explorer 12 observations. *Journal of Geophysical Research*, *72*(1), 171–183.

Sonnerup, B. U. O., & Scheible, M. (1998). Minimum and maximum variance analysis. In G. Paschmann, & P. Daly (Eds.), *Analysis methods for multi-spacecraft data* (pp. 185–220). Switzerland: International Space Science Institute, SR-001.

Torbert, R. B., Burch, J. L., Argall, M. R., Farrugia, C. J., Dors, I., Payne, D., et al. (2018). *Energetics within selected MMS encounters of electron diffusion regions* (pp. 10–14). Abstract SM33A-02 presented at the 2018 Fall Meeting, AGU, Washington, DC.

Torbert, R. B., Burch, J. L., Phan, T. D., Hesse, M., Argall, M. R., Shuster, J., et al. (2018), Electron-scale dynamics of the diffusion region during symmetric magnetic reconnection in space, *Science*, *362*(6421), 1391–1395, https://doi.org/10.1126/science.aat2998

Torbert, R. B., Dors, I., Argall, M. R., Genestreti, K. J., Burch, J. L., Farrugia, C. J., et al. (2020). A new method of 3-D magnetic field reconstruction. *Geophysical Research Letters*, *47*, e0027GL085. https://doi.org/10.1029/0027GL085542

Vasyliunas, V. (1975). Theoretical models of magnetic-field line merging. *Reviews of Geophysics*, *13*(1), 303–336. https://doi.org/10.1029/RG013i001p00303

Yao, S. T., Shi, Q. Q., Guo, R. L., Yao, Z. H., Tian, A. M., Degeling, A. W., et al. (2018). Magnetospheric Multiscale observations of electron scale magnetic peak. *Geophysical Research Letters*, *45*, 527–537. https://doi.org/10.1002/2017gl075711

Yao, S. T., Shi, Q. Q., Li, Z. Y., Wang, X. G., Tian, A. M., Sun, W. J., et al. (2016). Propagation of small size magnetic holes in the magnetospheric plasma sheet. *Journal of Geophysical Research: Space Physics*, *121*(6), 5510–5519. https://doi.org/10.1002/2016ja022741